

# Nonlinearity Characteristic of High Impedance Fault at Resonant Distribution Networks: Theoretical Basis to Identify the Faulty Feeder

Mingjie Wei, Hengxu Zhang, Fang Shi, Weijiang Chen, *Senior Member, IEEE*, Vladimir Terzija, *Fellow, IEEE*

**Abstract**— Feeder identification is indispensable for distribution networks to locate faults at a specific feeder, especially when measuring devices are insufficient for precise locations. For the high impedance fault (HIF), the feeder identification is much more complicated and related approaches are still in the early stage. This paper thoroughly and theoretically reveals the features of different feeders when a HIF happens at the resonant grounded neutral (RGN) network, which is the most challenging condition for feeder identification. Firstly, the diversity of nonlinearity existing in HIFs is explained from the aspect of energy. Then, the differences of nonlinearities of zero-sequence currents between healthy and faulty feeders are deduced theoretically. Variations of the detuning index and damping ratio that exist in industries are both considered. Afterward, these theoretical conclusions are verified by the HIF cases experimented in a real 10kV system. Finally, based on the theories, we discuss about why the existing approaches are not reliable enough, and suggest some improvements.

**Index Terms**—distribution networks, high impedance fault, feeder identification, resonant grounded neutral, nonlinearity

## I. INTRODUCTION

HIGH impedance faults (HIFs) account for more than 10% of the total fault accidents at medium-voltage (MV) distribution networks [1]. Generally, HIFs are the single-line-to-ground (SLG) faults, happening in overhead lines when the line conductor breaks off or sags to touch the high impedance grounding materials, like soil, concrete, asphalt, grass, and tree limb. The current amplitudes of HIFs are generally lower than 50A, or even below 1 A if conductors touch some materials with extremely high impedances [2]. In these cases, traditional overcurrent relays, which are still widely applied at nowadays networks, are unable to guarantee reliability. According to the early systematical staged tests carried out by Texas A&M University, only 17.5% of over 200 HIFs can be detected by traditional overcurrent relays [3]. When the faulted line establishes electrical conduction with the ground, the arc always ignites [4] as many air gaps exist between the two electrodes. As a result, the long-time existence of HIFs could raise the risks of fire and shock accidents. The severe fire hazards recently occurring in Australia, the United States, and Brazil, are confirmed to result from HIFs initially [5]. It further emphasizes the necessity

---

This work was supported by the National Key R&D Program of China (2017YFB0902800) and the Science and Technology Project of State Grid Corporation of China (52094017003D).

M. Wei, F. Shi and H. Zhang are all with the Key Laboratory of Power System Intelligent Dispatch and Control Ministry of Education, Shandong University, Jinan, 250061, China (e-mail: zhanghx@sdu.edu.cn

W. Chen is with the State Grid Corporation of China (e-mail:weijiang-chen@sgcc.cn).

V. Terzija is with the School of Electrical and Electronic Engineering, The University of Manchester, U.K. (e-mail: vladimir.terzija@manchester.ac.uk).

to detect and isolate HIFs.

Faulty feeder identification, which is a part of fault location, is still important for nowadays distribution system. At a practical network, a substation is commonly connected by several feeders, which further extend to a number of branches and supply for an area of dozens of kilometers. In order to locate the fault within a small area or even to a specific point, most techniques have to rely on the advanced devices which are deployed all over each feeder. However, the limitation of investment cannot always support that high-density equipment deployment. As a result, the identification of faulty feeder is still economical and practical, which only depends on the devices at the substation and the start of feeders. After the faulty feeder is identified, maintainers can fast patrol the specific transmission line for the fault position or switch off the whole feeder if necessary.

The feeder identification is commonly triggered by the detection of a HIF, where the latter technique has been researched over 40 years and achieved inspiring progress [6]-[8]. An approach to identify the faulty feeder is significantly dependent on the neutral type and the topology of a network. From a worldwide perspective, the distribution network is classified as four-wire and three-wire systems. The four-wire system is mainly applied in the United States, Canada, Brazil, Mexico, and Australia, where the network neutral is solidly grounded and a neutral line spreads over the network. For the three-wire system, which is applied in most of the other countries like China, Europe, and Japan [9],[10], isolated neutral (IN), resonant grounded neutral (RGN), and low-resistor grounded neutral (LRGN) are selectively applied on different conditions. Although the four-wire system possesses advantages like the economy, it faces significant problems in HIF diagnosis due to the interference of load current [11]. In the three-wire system, the zero-sequence current (ZSC) is close to zero at normal states and unaffected by (unbalanced) currents of loads and distributed generators (DGs), due to the isolation of load transformers [12]-[14]. In this way, fault features will not be submerged, and the reliability to identify the fault feeders can be significantly improved.

In this paper, only the three-wire system is discussed. Traditionally, fundamental phasors are the easiest way to isolate faults. Fig.1 presents the phasor diagram of fundamental ZSCs and zero-sequence voltage (ZSV) at the networks with three common neutrals. For IN (Fig.1a) and LRGN (Fig.1c) networks, faulty and healthy feeders can be easily distinguished just by fundamental phases and amplitudes. Based on this characteristic, algorithms in [14] and [15] are proposed to improve anti-noise ability further. However, at the RGN network (Fig.1b), the faulty feeder cannot be picked out only using phasors. For the low impedance fault (LIF), this problem can be solved by utilizing the direction of high-frequency transients [16],[17], which has been applied over

15 years in China [18]. However, for HIFs, the high-frequency transients are significantly suppressed, especially when the impedance reaches a certain high [9]. To solve this problem, in [9] and [12], a rule-based algorithm and a pattern-recognition-based algorithm are proposed, to identify HIF feeders with low-frequency transient projections and waveform distortions, respectively. However, their sensitivities are restricted by the variation of detuning of Petersen coil and nonlinear distortion.

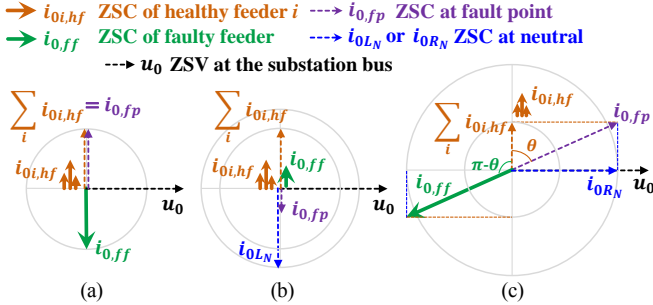


Fig.1 Phasors of fundamental ZSCs at different feeders: (a) IN network; (b) RGN network; (c) LRGN network.

An important reason that the reliability to identify HIF feeder is not high because most algorithms are based on the ‘phenomenon’ of some real cases or based on incomplete modelings. As a result, the algorithms cannot be useful for all fault conditions. The contributions of this paper are summarized as: 1) the diversity of HIF nonlinearity is theoretically introduced from the aspect of energy balance, which explains how the distortion of HIF current is affected by external environments. 2) the characteristics of healthy and faulty feeders at the RGN network are theoretically deduced. 3) The detuning index and damping ratio of Petersen coil are both considered, guaranteeing the industrial application. The theories are verified by the real HIFs experimented in a 10kV system. 4) Based on the conclusions, proposing more universally reliable approaches become possible. This paper also provides modifications for a well-known algorithm and show significant improvements.

## II. FEATURES OF HIF NONLINEARITY

### A. Analysis of Distortion Features by Energy

The nonlinearity of HIF is generally caused by the arcing process. For the arc column, the stored energy  $Q$  can be expressed according to the energy balance equation [19]:

$$\frac{dQ}{dt} = u \cdot i - P_{Loss} \quad (1)$$

where,  $P_{Loss}$  represents the power loss to the air, and  $u$ ,  $i$  represent the arc voltage and current, respectively. As the arc is nearly resistive, equation (1) can be further transformed as:

$$\frac{dQ}{dg_{arc}} \cdot \frac{dg_{arc}}{dt} = \frac{dQ}{dg_{arc}} \cdot \frac{-g_{arc}^2 \cdot dR_{arc}}{dt} = u \cdot i - P_{Loss} \quad (2)$$

where,  $g_{arc}$  is the arc conductance and  $R_{arc}$  is the arc resistance ( $R_{arc} = 1/g_{arc}$ ). Then, (2) can be written as:

$$\frac{1}{R_{arc}} \frac{dR_{arc}}{dt} = \frac{P_{Loss} - u \cdot i}{g_{arc} \cdot dQ/dg_{arc}} = \frac{1}{\tau} (P_{Loss} - u \cdot i) \quad (3)$$

where,  $\tau = g_{arc} \cdot dQ/dg_{arc}$ . Then,  $R_{arc}$  is expressed as:

$$R_{arc} = e^{\int \frac{1}{\tau} (P_{Loss} - u \cdot i) dt} \quad (4)$$

Arcing nonlinearity is essentially caused by  $R_{arc}$ , while  $R_{arc}$  is affected by the energy conversion in the arc gap. Because the input power  $u \cdot i$  is the dependent variable, the nonlinearity of  $R_{arc}$  is only affected by  $\tau$  and  $P_{Loss}$ . Herein,  $P_{Loss}$  reflects the energy dissipation ability in the arc column, which is closely related to the movability and thermal conductivity of the air space and ground medium. About  $\tau$ , it reflects how fast arc resistance changes as the stored energy.

Simulations are conducted to figure out how  $R_{arc}$  is affected by the two parameters. Some examples are shown in Fig.2, where  $P_{Loss}$  and  $\tau$  are assumed as constants for simplification, just like the Mayr model. For the HIF simulation, RMS of current is controlled by a large linear resistor  $R_T$ , which is in series with the nonlinear  $R_{arc}$ .

$R_{arc}$  exhibits as a ‘spike’ curve twice in each cycle and reaches the maximum when  $dR_{arc}/dt = 0$ , i.e.,  $u \cdot i = P_{Loss}$ . Because  $u \cdot i = 0$  at the zero-crossing of current, the maximal  $R_{arc}$  will show increasing offsets relative to zero-crossings when  $P_{Loss}$  increases, like from Fig.2(a) to (c). Besides,  $P_{Loss}$  and  $\tau$  respectively determines how long and how fast  $R_{arc}$  increases, which together affect the level of  $R_{arc}$ .

In conclusion, the external environment of HIF, like material, humidity, and structure of the ground surface, affects the energy conversion of arc. Then, the energy conversion, reflected by  $P_{Loss}$  and  $\tau$ , controls the curve of  $R_{arc}$ . Finally,  $R_{arc}$  determines the nonlinearity and distortion of fault current, the specific relationship between which has been summarized in our previous work [19].

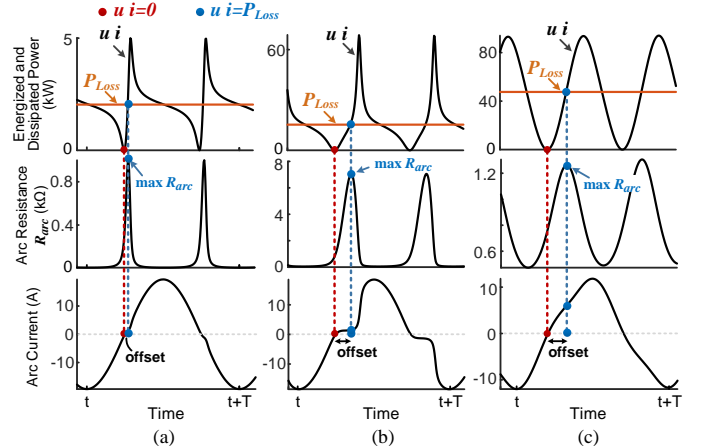


Fig.2 Effects of  $P_{Loss}$  (kW) and  $\tau$  (kW·s) on the waveform distortion: (a)  $P_{Loss}=2$ ,  $\tau=0.3$ ; (b)  $P_{Loss}=16$ ,  $\tau=1.67$ ; (c)  $P_{Loss}=46$ ,  $\tau=3.3$ .

### B. Artificial Experiments in A Real 10kV System

Artificial HIFs have been tested at a real 10kV 50Hz distribution network, the topology of which is shown in Fig.3. In this paper, these real HIFs are used to explain the practical fault features and verify the theories.

The neutral of the RGN network is grounded with a tunable Petersen coil. There are four feeders under operations and they are with different combinations of underground cables and overhead lines, as shown in Fig.3. Specific lengths of feeders are also marked in the figure. HIFs are tested after grounding the energized lines to different surfaces, including soil, cement, asphalt, and grass, etc. The surface humidity is simply classified as wet and dry. Signals are measured by devices with 6.4 kHz sampling frequency, which are deployed at the beginning

of each feeder (M1~M4), outside the substation transformer (M5), and at the fault point (Mf).

Currents of some real HIFs are the black curves presented in Fig.4. They exhibit and verify the diversity of current distortions as theoretically discussed in Section II.A. This diversity has to be considered in the HIF diagnosis, especially for the slight distortions like Fig.4 (d)-(e), or large distortion offsets in Fig.4 (f)-(g).

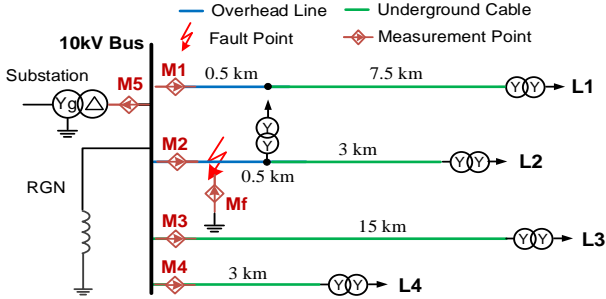


Fig.3 Topology of a real 10 kV distribution network.

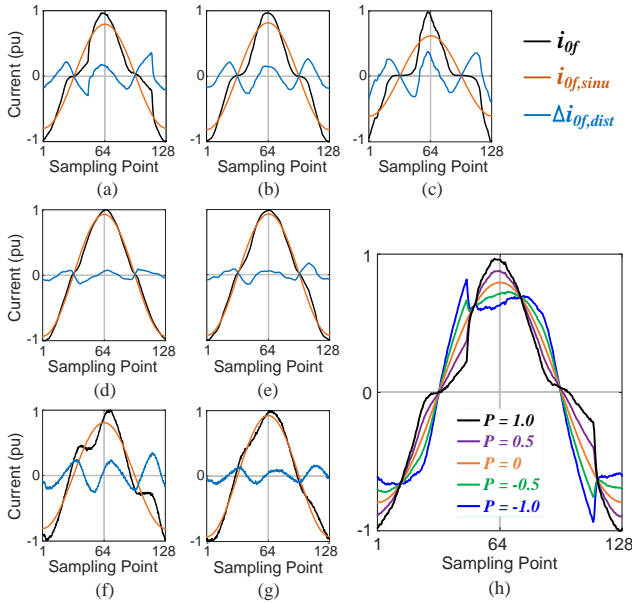


Fig.4 Sinusoidal and distortional components of HIF current experimented in a real 10kV distribution network: (a) wet asphalt concrete; (b) dry soil; (c) wet soil; (d) wet cement; (e) wet asphalt concrete; (f) dry grass; (g) wet grass; (h) the current waveforms when the distortional content varies.

### III. DISTORTION DIFFERENCES BETWEEN FEEDERS

For the RGN network, distortion differences of ZSCs at healthy and faulty feeders are theoretically deduced in this section.

#### A. Sinusoidal Component and Distortional Component

It is known that any signal can be resolved as the linear superposition of sine waves with different frequencies. The ZSC of HIF at the fault point, denoted as  $i_{of}$ , can be written as:

$$i_{of} = i_{of,sinu} + \Delta i_{of,dist}$$

$$\begin{cases} i_{of,sinu} = A_0 \sin(\omega_0 t + \varphi_0) \\ \Delta i_{of,dist} \approx \sum_{k=2}^m \Delta i_{of,dist}^{(H,k)} = \sum_{k=2}^m A_{H,k} \sin(k\omega_0 t + \varphi_{H,k}) \end{cases} \quad (5)$$

where the sinusoidal component and distortional component of  $i_{of}$  are defined as  $i_{of,sinu}$  and  $\Delta i_{of,dist}$ , respectively.  $\omega_0$ ,

$\varphi_0$ , and  $A_0$  are the fundamental radian frequency, phase (angle), and peak amplitude, respectively.  $\varphi_{H,k}$  and  $A_{H,k}$  represent the phase and peak amplitude of the  $k$ th harmonic distortional component ( $\Delta i_{of,dist}^{(H,k)}$ ), respectively. The white noise, impulse noise, and inter-harmonics are neglected as distortions are mainly caused by the low-order integer harmonics.

In Fig.4, the  $i_{of}$  of some real HIFs experimented in the aforementioned 10kV system are presented, together with their two components. Specifically,  $i_{of,sinu}$  is achieved by FFT while  $\Delta i_{of,dist}$  is achieved by  $i_{of} - i_{of,sinu}$ . Take Fig.4 (a) as an example and change the content of  $\Delta i_{of,dist}$  as:

$$i_{0X} = i_{of,sinu} + P \cdot \Delta i_{of,dist} \quad (6)$$

Respectively set  $P$  as -1, -0.5, 0, 0.5, 1, and the corresponding  $i_{0X}$  are shown in Fig.4 (h). Define the conditions when  $P > 0$  as ‘positive superposition’, and as ‘negative superposition’ when  $P < 0$ . As a result,  $i_{of}$  is always with ‘positive superposition’. The currents with different superpositions will present significantly different distortion and the opposite phases of harmonic components.

#### B. Differences Between Feeders

##### 1) Expressions of Sinusoidal and Distortional Components:

Fig.5 is an equivalent zero-sequence circuit of an RGN network with multiple feeders [9], where:

$C_{0i}$	Equivalent zero-sequence line-to-ground capacitance of feeder $i$ ( $i=1,2,\dots,n$ )	$u_f$	Equivalent virtual voltage source, which has the same amplitude with and opposite phase to the pre-fault phase-to-ground voltage at the fault point
$L$	Equivalent zero-sequence inductance of the Petersen coil (3 times the coil inductance)	$u_{ob}$	ZSV at the substation bus
$R_{HIF}$	Equivalent zero-sequence resistance of fault (3 times the grounding resistance)	$i_{of}$	ZSC at the fault point
$i_{0L}$	ZSC flowing through the Petersen coil	$i_{0i}$	ZSC at the beginning of feeder $i$
		$i_{0C_{0i}}$	ZSC of the line-to-ground capacitance at feeder $i$

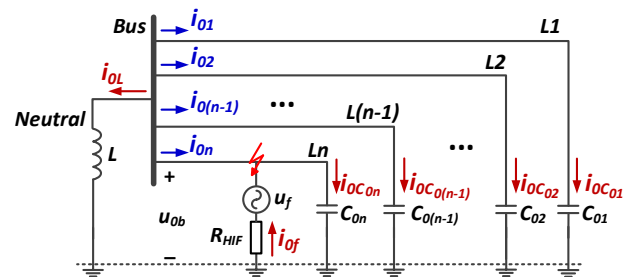


Fig.5 Equivalent zero-sequence circuit of a multi-feeder resonant network.

Set a HIF in feeder  $n$ , then  $i_{of}$  can be expressed as:

$$i_{of} = i_{0L} + \sum_{i=1}^n i_{0C_{0i}} \quad (7)$$

Then,  $i_{0L}$  and  $i_{0C_{0i}}$  are also respectively resolved into a sinusoidal component and a distortional component:

$$i_{of} = i_{0L,sinu} + \sum_{k=2}^m \Delta i_{0L,dist}^{(H,k)} + \sum_{i=1}^n \left( i_{0C_{0i},sinu} + \sum_{k=2}^m \Delta i_{0C_{0i},dist}^{(H,k)} \right) \quad (8)$$

where the sinusoidal and distortional components of  $i_{0L}$  and  $i_{0C_{0i}}$  are accordingly expressed. Further, according to Fig.5:

$$\begin{aligned}
u_{0b} &= \frac{1}{C_{0i}} \int i_{0c_{0i}} dt = \frac{1}{C_{0\Sigma}} \int \sum_{i=1}^n i_{0c_{0i}} dt = L \frac{di_{0L}}{dt} \\
\Rightarrow u_{0b} &= u_{0b,sinu} + \sum_{k=2}^m \Delta u_{0b,dist}^{(H,k)} \\
&= \frac{1}{C_{0i}} \int \left( i_{0c_{0i},sinu} + \sum_{k=2}^m \Delta i_{0c_{0i},dist}^{(H,k)} \right) dt \\
&= \frac{1}{C_{0\Sigma}} \int \sum_{i=1}^n \left( i_{0c_{0i},sinu} + \sum_{k=2}^m \Delta i_{0c_{0i},dist}^{(H,k)} \right) dt \\
&= L \frac{d \left( i_{0L,sinu} + \sum_{k=2}^m \Delta i_{0L,dist}^{(H,k)} \right)}{dt}
\end{aligned} \tag{9}$$

where,  $C_{0\Sigma} = \sum_{i=1}^n C_{0i}$ .

It is known that the sine waves with different frequencies are mutually orthogonal. It means the sinusoidal and distortional components, as well as different orders of harmonics, cannot transform into each other. As a result, based on (5)-(9), we have:

$$\begin{cases} i_{0f,sinu} = i_{0L,sinu} + \sum_{i=1}^n i_{0c_{0i},sinu} \\ u_{0b,sinu} = \frac{\int i_{0c_{0i},sinu} dt}{C_{0i}} = \frac{\int \sum_{i=1}^n i_{0c_{0i},sinu} dt}{C_{0\Sigma}} = L \frac{di_{0L,sinu}}{dt} \end{cases} \tag{10}$$

$$\begin{cases} \Delta i_{0f,dist}^{(H,k)} = \Delta i_{0L,dist}^{(H,k)} + \sum_{i=1}^n \Delta i_{0c_{0i},dist}^{(H,k)} \\ \Delta u_{0b,dist}^{(H,k)} = \frac{\int \Delta i_{0c_{0i},dist}^{(H,k)} dt}{C_{0i}} = \frac{\int \sum_{i=1}^n \Delta i_{0c_{0i},dist}^{(H,k)} dt}{C_{0\Sigma}} = L \frac{d\Delta i_{0L,dist}^{(H,k)}}{dt} \end{cases} \tag{11}$$

It means the superposition principle in linear systems is still valid for the sinusoidal and distortional components.

For  $i_{0f}$ , when the phase of its sinusoidal component  $i_{0f,sinu}$  is  $\varphi_0$  as defined in (5), the phases of  $i_{0L,sinu}$  and  $i_{0c_{0i},sinu}$  should respectively be  $\varphi_0$  and  $\varphi_0 + \pi$  according to (10). For  $\Delta i_{0f,dist}^{(H,k)}$ , according to (5) and (11), it can be expressed as:

$$\begin{aligned}
\Delta i_{0f,dist}^{(H,k)} &= \Delta i_{0L,dist}^{(H,k)} + \sum_{i=1}^n \Delta i_{0c_{0i},dist}^{(H,k)} \\
&= \Delta i_{0L,dist}^{(H,k)} + LC_{0\Sigma} \frac{d^2 \Delta i_{0L,dist}^{(H,k)}}{dt^2} = A_{H,k} \sin(k\omega_0 t + \varphi_{H,k})
\end{aligned} \tag{12}$$

This second-order non-homogeneous linear (NHL) equation

$$i_{0n} = -i_{0f} + i_{0c_{0n}} = - \left( i_{0L} + \sum_{i=1}^{n-1} i_{0c_{0i}} \right) = - \left( i_{0L,sinu} + \sum_{i=1}^{n-1} i_{0c_{0i},sinu} \right) - \sum_{k=2}^m \left( \Delta i_{0L,dist}^{(H,k)} + \sum_{i=1}^{n-1} \Delta i_{0c_{0i},dist}^{(H,k)} \right) \tag{17}$$

$$\begin{aligned}
&= - \left( A_{ML} - \sum_{i=1}^{n-1} A_{MC_{0i}} \right) \sin(\omega_0 t + \varphi_0) - \sum_{k=2}^m \left[ 1 + \frac{k^2 \omega_0^2 LC_{0n}}{1 - k^2 \omega_0^2 LC_{0\Sigma}} \right] A_{H,k} \sin(k\omega_0 t + \varphi_{H,k}) \\
&= \frac{\omega_0^2 L (C_{0\Sigma} - C_{0n}) - 1}{\omega_0^2 LC_{0\Sigma} - 1} (-i_{0f}) - \sum_{k=2}^m \frac{\omega_0^2 LC_{0n} (1 - k^2)}{(\omega_0^2 LC_{0\Sigma} - 1)(1 - k^2 \omega_0^2 LC_{0\Sigma})} A_{H,k} \sin(k\omega_0 t + \varphi_{H,k}) \\
&= \left( \frac{1}{-v} \right) \left[ \left( -v + \frac{C_{0n}}{C_{0\Sigma}} \right) (-i_{0f}) + \sum_{k=2}^m \frac{C_{0n}}{C_{0\Sigma}} \frac{1 - k^2}{1 - k^2 \omega_0^2 LC_{0\Sigma}} A_{H,k} \sin(k\omega_0 t + \varphi_{H,k}) \right]
\end{aligned}$$

$$i_{0i(i \neq n)} = i_{0c_{0i}} = i_{0c_{0i},sinu} + \sum_{k=2}^m \Delta i_{0c_{0i},dist}^{(H,k)} = \frac{C_{0i}}{-vC_{0\Sigma}} \left[ (-i_{0f}) + \sum_{k=2}^m \frac{1 - k^2}{1 - k^2 \omega_0^2 LC_{0\Sigma}} A_{H,k} \sin(k\omega_0 t + \varphi_{H,k}) \right] \tag{18}$$

$$i_{0L} = i_{0L,sinu} + \sum_{k=2}^m \Delta i_{0L,dist}^{(H,k)} = \left( \frac{1}{-v} \right) \left[ (1 - v) i_{0f} - \sum_{k=2}^m \frac{1 - k^2}{1 - k^2 \omega_0^2 LC_{0\Sigma}} A_{H,k} \sin(k\omega_0 t + \varphi_{H,k}) \right] \tag{19}$$

In the final expressions of (17)~(19), when  $k \geq 2$ , it has:

$$\frac{1 - k^2}{1 - k^2 \omega_0^2 LC_{0\Sigma}} \in \left( \frac{1}{\omega_0^2 LC_{0\Sigma}}, \frac{3}{4\omega_0^2 LC_{0\Sigma} - 1} \right) \tag{20}$$

can be solved as:

$$\begin{cases} \Delta i_{0L,dist}^{(H,k)} = \frac{1}{1 - k^2 \omega_0^2 LC_{0\Sigma}} A_{H,k} \sin(k\omega_0 t + \varphi_{H,k}) \\ \Delta i_{0c_{0i},dist}^{(H,k)} = \frac{-k^2 \omega_0^2 LC_{0i}}{1 - k^2 \omega_0^2 LC_{0\Sigma}} A_{H,k} \sin(k\omega_0 t + \varphi_{H,k}) \end{cases} \tag{13}$$

2) Expressions of ZSCs at Different Feeders:

For an RGN network, the detuning index  $v$  reflects the ability of the Petersen coil to compensate for the capacitive currents of the network [9], and it is expressed as:

$$v = \frac{\sum_{i=1}^n A_{MC_{0i}} - A_{ML}}{\sum_{i=1}^n A_{MC_{0i}}} = 1 - \frac{1}{\omega_0^2 LC_{0\Sigma}} = \frac{\omega_0^2 LC_{0\Sigma} - 1}{\omega_0^2 LC_{0\Sigma}} \tag{14}$$

where,  $A_{MC_{0i}}$  and  $A_{ML}$  represent the peak amplitude of  $i_{0c_{0i},sinu}$  and  $i_{0L,sinu}$ , respectively. Ideally,  $v \in [-0.1, 0)$  so that  $\omega_0^2 LC_{0\Sigma} \in [0.9091, 1)$ . Then, with (14), ratios of the following peak amplitudes can be expressed:

$$\begin{cases} \frac{A_{ML} - \sum_{i=1}^{n-1} A_{MC_{0i}}}{A_{ML} - \sum_{i=1}^n A_{MC_{0i}}} = \frac{\omega_0^2 L (C_{0\Sigma} - C_{0n}) - 1}{\omega_0^2 LC_{0\Sigma} - 1} = 1 - \frac{C_{0n}}{vC_{0\Sigma}} \\ \frac{A_{MC_{0i}}}{A_{ML} - \sum_{i=1}^n A_{MC_{0i}}} = \frac{\omega_0^2 LC_{0i}}{1 - \omega_0^2 LC_{0\Sigma}} = \frac{C_{0i}}{-vC_{0\Sigma}} \\ \frac{A_{ML}}{A_{ML} - \sum_{i=1}^n A_{MC_{0i}}} = \frac{1}{1 - \omega_0^2 LC_{0\Sigma}} = 1 - \frac{1}{v} \end{cases} \tag{15}$$

When  $i_{0f}$  is expressed in the form of (16), the ZSC at the start of the faulty feeder ( $i_{0n}$ ), healthy feeders ( $i_{0i(i \neq n)}$ ), and substation feeder ( $i_{0L}$ ), can be respectively expressed as (17)-(19), where (14) and (15) are used during the deducing. For the sake of brevity, we only present the deducing process of (17), and omit those of (18) and (19).

$$\begin{aligned}
i_{0f} &= i_{0L} + \sum_{i=1}^n i_{0c_{0i}} = i_{0f,sinu} + \Delta i_{0f,dist} \\
&= \left( A_{ML} - \sum_{i=1}^n A_{MC_{0i}} \right) \sin(\omega_0 t + \varphi_0) + \sum_{k=2}^m A_{H,k} \sin(k\omega_0 t + \varphi_{H,k})
\end{aligned} \tag{16}$$

After  $\omega_0^2 LC_{0\Sigma}$  is determined as a value in [0.9091, 1), the widest range of  $\frac{1 - k^2}{1 - k^2 \omega_0^2 LC_{0\Sigma}}$  is [1.100, 1.138]. For the convenience, simplify  $\frac{1 - k^2}{1 - k^2 \omega_0^2 LC_{0\Sigma}}$  as a constant. As a result, (17)~(19)

are rewritten as (21)~(23), respectively:

$$\begin{aligned} i_{0n} &= \left(\frac{1}{-v}\right) [P_1(-i_{0f}) + P_2\Delta i_{0f,dist}] \\ &= -\left(\frac{1}{-v}\right) P_1 \left[ i_{0f,sinu} + \frac{P_1 - P_2}{P_1} \Delta i_{0f,dist} \right] \end{aligned} \quad (21)$$

$$\begin{aligned} i_{0i(i \neq n)} &= \left(\frac{1}{-v}\right) [P_3(-i_{0f}) + P_4\Delta i_{0f,dist}] \\ &= -\left(\frac{1}{-v}\right) P_3 \left[ i_{0f,sinu} + \frac{P_3 - P_4}{P_3} \Delta i_{0f,dist} \right] \end{aligned} \quad (22)$$

$$\begin{aligned} i_{0L} &= \left(\frac{1}{-v}\right) [P_5 i_{0f} - P_6 \Delta i_{0f,dist}] \\ &= \left(\frac{1}{-v}\right) P_5 \left[ i_{0f,sinu} + \frac{P_5 - P_6}{P_5} \Delta i_{0f,dist} \right] \end{aligned} \quad (23)$$

where,  $P_1 \sim P_6$  are all positive constants and expressed as:  $P_1 = -v + \frac{C_{0n}}{C_{0\Sigma}}$ ,  $P_2 = \frac{C_{0n}}{C_{0\Sigma}} \cdot \frac{1-k^2}{1-k^2\omega_0^2LC_{0\Sigma}}$ ,  $P_3 = \frac{C_{0i}}{C_{0\Sigma}}$ ,  $P_4 = \frac{C_{0i}}{C_{0\Sigma}} \cdot \frac{1-k^2}{1-k^2\omega_0^2LC_{0\Sigma}}$ ,  $P_5 = 1 - v$ , and  $P_6 = \frac{1-k^2}{1-k^2\omega_0^2LC_{0\Sigma}}$ , respectively.

Obviously, (21)~(23) are all in the form of (5). As  $P_3 - P_4 < 0$ ,  $i_{0i(i \neq n)}$  is with the negative superposition, which is opposite to that of  $i_{0f}$ . According to (20),  $P_6 = \frac{1-k^2}{1-k^2\omega_0^2LC_{0\Sigma}} > \frac{1}{\omega_0^2LC_{0\Sigma}} = 1 - v = P_5$ , so  $P_5 - P_6 < 0$ . Therefore, the superposition characteristic of  $i_{0L}$  is also opposite to that of  $i_{0f}$ . To identify the faulty feeder, the superposition characteristic of  $i_{0n}$  would better be the same as  $i_{0f}$ , i.e., the positive superposition. To meet this purpose, the  $P_1 - P_2$  in (24) should be larger than 0.

$$\begin{aligned} P_1 - P_2 &= -v + \frac{C_{0n}}{C_{0\Sigma}} - \frac{C_{0n}}{C_{0\Sigma}} \cdot \frac{1-k^2}{1-k^2\omega_0^2LC_{0\Sigma}} \\ &= (-v) \frac{1-k^2\omega_0^2L(C_{0\Sigma} - C_{0n})}{1-k^2\omega_0^2LC_{0\Sigma}} \end{aligned} \quad (24)$$

To make  $P_1 - P_2 > 0$ , it should be satisfied that  $1 - k^2\omega_0^2L(C_{0\Sigma} - C_{0n}) < 0$ , i.e.,  $\frac{C_{0n}}{C_{0\Sigma}} < 1 - \frac{1}{k^2\omega_0^2LC_{0\Sigma}} = 1 - \frac{1-v}{k^2}$ . When  $v \geq -0.1$  and  $k \geq 2$ , it should be satisfied that  $1 - \frac{1-v}{k^2} \geq 0.725$ . As a result, only when  $\frac{C_{0n}}{C_{0\Sigma}} < 0.725$  can make  $P_1 - P_2 > 0$  always valid on the condition of  $v \geq -0.1$ . The larger the  $\frac{C_{0n}}{C_{0\Sigma}}$ , the smaller the  $P_1 - P_2$  and the weaker the distortion of  $i_{0n}$ . In most cases, HIFs happen in overhead lines instead of underground cables, and there are more than one feeders connected to a substation, so  $\frac{C_{0n}}{C_{0\Sigma}} \ll 0.725$ .

In summary, at the RGN network, the ZSCs at healthy and faulty feeders are with the inverse superposition characteristics. It makes significant differences between their features. For example, phases of the same harmonic components are completely the opposite, and the current distortions also present notably different shapes, as illustrated in Fig.4(h).

### 3) Verification:

A real HIF, which is experimented in the 10kV system and grounded to wet soil, is used to verify the above conclusion that is based on (21)~(23). Fig.6 (a) shows the ZSCs measured at M1~M5 and Mf. Positions of these devices have been introduced in Section II.B. The verification is conducted as follows:

Step 1: Resolve  $i_{0f}$  (i.e.,  $i_{0Mf}$  for this case) into a sinusoidal component and a distortional component, as in Fig.6 (b).

Step 2: Use FFT to calculate the peak amplitudes of sinusoidal components for each ZSC, i.e.,:  $A_{Mi(i=1,2,\dots,5,f)}$ .

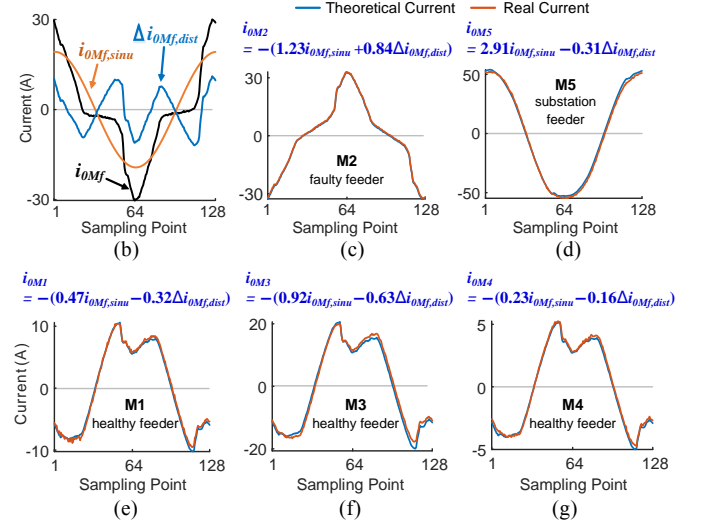
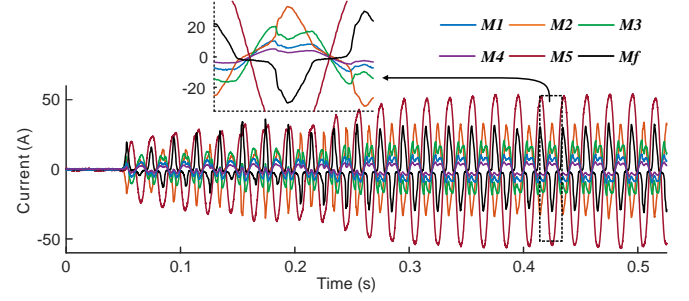


Fig.6 Verification of the theoretically calculated ZSCs by a real HIF. (a) ZSCs of a real HIF; (b) sinusoidal and distortional components of the ZSC at the fault point; (c)~(g) comparison between the theoretical and real ZSCs at the faulty feeder, substation feeder, and healthy feeders, respectively.

Step 3: Use these amplitudes to calculate  $v$  according to (14). According to (20), simplify  $\frac{1-k^2}{1-k^2\omega_0^2LC_{0\Sigma}}$  as a constant equaling  $\left(\frac{1}{\omega_0^2LC_{0\Sigma}} + \frac{3}{4\omega_0^2LC_{0\Sigma}-1}\right)/2$ .

Step 4: Bring the parameters calculated in Step 3 back into (21)~(23), and calculate the theoretical ZSCs of each feeder.

The theoretical waveforms and the real waveforms in Fig.6 (a) are compared in Fig.6 (c)~(g), respectively for each feeder. The expressions of (21)~(23) are calculated and presented above the corresponding figure. As is shown, the theoretical curves are perfectly consistent with the real ones, which validate the correctness of the deducing in this section.

## IV. CALIBRATION AFTER CONSIDERING DAMPING RATIO

### A. Existence of Resistive Components

At the practical network, there always exist resistive components in  $i_{0f}$ , which are mainly caused by the resistance of the Petersen coil and line-to-ground resistance. Therefore, the equivalent circuit in Fig.5 can be transformed as Fig.7.

In some cases, resistive components are so small, so that the conclusions in the previous section are still valid, like the case in Fig.6. However, as the decrease of  $v$ ,  $i_{0L}$  is compensated to a small value, and  $i_{0R}$  cannot be neglected anymore. For example, Fig.8 (a) shows the ZSCs of another real HIF, which is grounded to wet asphalt. Affected by  $i_{0R}$ , the ZSC of faulty feeder shows obvious phase deviation compared to those of healthy feeders. Due to  $i_{0R_{0i}}$ , phases of ZSCs at the healthy

feeders are also a bit different from each other.

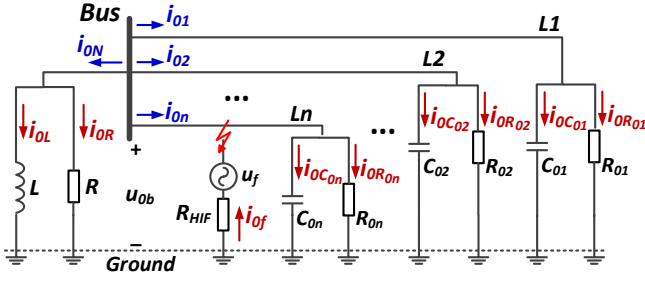


Fig.7 Equivalent zero-sequence circuit after considering damping ratio.

The blue curves in Fig.8 (c)~(g) represent the theoretical ZSCs calculated by (21)~(23). Obviously, both the phases and distortion shapes are not consistent with the real ones at all. Therefore, calibrations are required.

### B. Expressions of ZSCs at Different Feeders

The damping ratio, denoted as  $d$ , is defined as:

$$d = \frac{A_{MR} + \sum_{i=1}^n A_{MR_{oi}}}{\sum_{i=1}^n A_{MC_{oi}}} = \frac{1/R + \sum_{i=1}^n 1/R_{oi}}{\omega_0 C_{0\Sigma}} = \frac{1}{\omega_0 R_{\Sigma} C_{0\Sigma}} \quad (25)$$

where,  $\frac{1}{R_{\Sigma}} = \frac{1}{R} + \sum_{i=1}^n \frac{1}{R_{oi}}$ ;  $A_{MR}$  and  $A_{MR_{oi}}$  represent the peak amplitudes of  $i_{0R,sinu}$  and  $i_{0R_{oi},sinu}$ , respectively. For an RGN network,  $d$  and  $v$  are two significant parameters to reflect the compensation ability for the fault current.

$$i_{0n} = \sqrt{\frac{(c_n - v)^2 + d^2 (r_{R_{on}} - 1)^2}{v^2 + d^2}} \overrightarrow{E_{x,sinu}} \cdot e^{j\theta_{sinu}} + \sum_{k=2}^m \sqrt{\frac{(c_n - v_{H,k})^2 + d_{H,k}^2 (r_{R_{on}} - 1)^2}{v_{H,k}^2 + d_{H,k}^2}} \overrightarrow{E_{x,dist}}^{(H,k)} \cdot e^{j\theta_{dist}^{(H,k)}} \quad (28)$$

$$\theta_{sinu} = \pi + \arctan \left[ \frac{dc_n - r_{R_{on}} dv}{c_n v - v^2 - (1 - r_{R_{on}}) d^2} \right], \quad \theta_{dist}^{(H,k)} = \begin{cases} \arctan \left[ \frac{d_{H,k} c_n - r_{R_{on}} d_{H,k} v_{H,k}}{c_n v_{H,k} - v_{H,k}^2 - (1 - r_{R_{on}}) d_{H,k}^2} \right], & c_n > v_{H,k} + (1 - r_{R_{on}}) d_{H,k}^2 / v_{H,k} \\ \pi + \arctan \left[ \frac{d_{H,k} c_n - r_{R_{on}} d_{H,k} v_{H,k}}{c_n v_{H,k} - v_{H,k}^2 - (1 - r_{R_{on}}) d_{H,k}^2} \right], & c_n \leq v_{H,k} + (1 - r_{R_{on}}) d_{H,k}^2 / v_{H,k} \end{cases}$$

$$i_{0i(i \neq n)} = \sqrt{\frac{r_{R_{oi}}^2 d^2 + c_i^2}{v^2 + d^2}} \overrightarrow{E_{x,sinu}} \cdot e^{j\theta_{sinu}} + \sum_{k=2}^m \sqrt{\frac{r_{R_{oi}}^2 d_{H,k}^2 + c_i^2}{v_{H,k}^2 + d_{H,k}^2}} \overrightarrow{E_{x,dist}}^{(H,k)} \cdot e^{j\theta_{dist}^{(H,k)}} \quad (29)$$

$$\theta_{sinu} = \begin{cases} \arctan \left( \frac{c_i d - r_{R_{oi}} dv}{c_i v + r_{R_{oi}} d^2} \right), & c_i v + r_{R_{oi}} d^2 > 0 \\ \pi + \arctan \left( \frac{c_i d - r_{R_{oi}} dv}{c_i v + r_{R_{oi}} d^2} \right), & c_i v + r_{R_{oi}} d^2 \leq 0 \end{cases}$$

$$\theta_{dist}^{(H,k)} = \arctan \left( \frac{c_i d_{H,k} - r_{R_{oi}} d_{H,k} v_{H,k}}{c_i v_{H,k} + r_{R_{oi}} d_{H,k}^2} \right)$$

$$i_{0N} = -\sqrt{\frac{(v^2 + d^2)[(1 - v)^2 + r_R^2 d^2]}{v^2 + d^2}} \overrightarrow{E_{x,sinu}} \cdot e^{j\theta_{sinu}} - \sum_{k=2}^m \sqrt{\frac{(v_{H,k}^2 + d_{H,k}^2)[(1 - v_{H,k})^2 + r_R^2 d_{H,k}^2]}{v_{H,k}^2 + d_{H,k}^2}} \overrightarrow{E_{x,dist}}^{(H,k)} \cdot e^{j\theta_{dist}^{(H,k)}} \quad (30)$$

$$\theta_{sinu} = \pi + \arctan \left[ \frac{d(1 - v) + r_R dv}{v(1 - v) - r_R d^2} \right], \quad \theta_{dist}^{(H,k)} = \begin{cases} \arctan \left[ \frac{d_{H,k}(1 - v_{H,k}) + r_R d_{H,k} v_{H,k}}{v_{H,k}(1 - v_{H,k}) - r_R d_{H,k}^2} \right], & v_{H,k}(1 - v_{H,k}) > r_R d_{H,k}^2 \\ \pi + \arctan \left[ \frac{d_{H,k}(1 - v_{H,k}) + r_R d_{H,k} v_{H,k}}{v_{H,k}(1 - v_{H,k}) - r_R d_{H,k}^2} \right], & v_{H,k}(1 - v_{H,k}) \leq r_R d_{H,k}^2 \end{cases}$$

According to (26) and (28)~(30), after resolving  $i_{0f}$  into  $\overrightarrow{E_{x,sinu}}$  and  $\sum_{k=2}^m \overrightarrow{E_{x,dist}}^{(H,k)}$ , the ZSCs at different feeders can be achieved by counterclockwise rotating  $\overrightarrow{E_{x,sinu}}$  and each  $\overrightarrow{E_{x,dist}}^{(H,k)}$  by different angles, multiplying them by different multipliers, and finally, linearly adding all the components up.

### C. Verification

The real HIF in Fig.8 (a) is used to verify the correctness of

The deducing process is similar to Section III. However, the difference is that  $i_{0R}$  and  $i_{0R_{oi}}$  are included in (7)~(11). Define  $\overrightarrow{E_{x,sinu}} = A_0 \sin(\omega_0 t + \varphi_0)$  and  $\overrightarrow{E_{x,dist}}^{(H,k)} = A_{H,k} \sin(k\omega_0 t + \varphi_{H,k})$ , then the  $i_{0f}$  in (5) can be expressed as:

$$i_{0f} = i_{0f,sinu} + \sum_{k=2}^m \Delta i_{0f,dist}^{(H,k)} = \overrightarrow{E_{x,sinu}} + \sum_{k=2}^m \overrightarrow{E_{x,dist}}^{(H,k)} \quad (26)$$

Afterward, like (12), establish the NHL equations for sinusoidal and distortional components, respectively:

$$\begin{cases} i_{0f,sinu} = i_{0L,sinu} + \frac{L}{R_{\Sigma}} \frac{di_{0L,sinu}}{dt} + LC_{0\Sigma} \frac{d^2 i_{0L,sinu}}{dt^2} \\ = A_0 \sin(\omega_0 t + \varphi_0) = \overrightarrow{E_{x,sinu}} \\ \Delta i_{0f,dist}^{(H,k)} = \Delta i_{0L,dist}^{(H,k)} + \frac{L}{R_{\Sigma}} \frac{d\Delta i_{0L,dist}^{(H,k)}}{dt} + LC_{0\Sigma} \frac{d^2 \Delta i_{0L,dist}^{(H,k)}}{dt^2} \\ = A_{H,k} \sin(k\omega_0 t + \varphi_{H,k}) = \overrightarrow{E_{x,dist}}^{(H,k)} \end{cases} \quad (27)$$

Solve the NHL equations and obtain the two components of  $i_{0L}$ ,  $i_{0R}$ ,  $i_{0C_{oi}}$ , and  $i_{0R_{oi}}$ , respectively. Then, the ZSCs at the faulty feeder ( $i_{0n} = -i_{0f} + i_{0C_{on}} + i_{0R_{on}}$ ), the healthy feeders ( $i_{0i} = i_{0C_{oi}} + i_{0R_{oi}}$ ,  $i \neq n$ ), and the substation feeder ( $i_{0N} = i_{0L} + i_{0R}$ ) are respectively expressed as (28)~(30), where  $v_{H,k} = 1 - \frac{1-v}{k^2}$ ,  $d_{H,k} = \frac{d}{k}$ ,  $r_{R_{oi}} = \frac{R_{\Sigma}}{R_{oi}}$ ,  $r_R = \frac{R_{\Sigma}}{R}$  and  $c_i = \frac{C_{oi}}{C_{0\Sigma}}$ . Due to the page limitation, detailed deducing is omitted.

(28)~(30), the coefficients of which are calculated as follows:

Step 1: Resolve  $i_{0f}$  (i.e.,  $i_{0Mf}$  for this case) into  $i_{0f,sinu}$  and  $\Delta i_{0f,dist}$  as in Fig.8 (b), which are represented as  $\overrightarrow{E_{x,sinu}}$  and  $\sum_{k=2}^m \overrightarrow{E_{x,dist}}^{(H,k)}$ , respectively.

Step 2: Fig.9 is the phasor diagram when considering the damping ratio. Use FFT to calculate the phases of  $u_{ob,sinu}$ ,  $i_{0i,sinu}(i \neq n)$ , and  $i_{0N,sinu}$  as  $\varphi_{ob}$ ,  $\varphi_{oi}$ , and  $\varphi_{0N}$ , respectively.

Then, the phases of  $i_{0C_{oi},sinu}$  and  $i_{0L,sinu}$  can be estimated as  $\varphi_{0b} + \frac{\pi}{2}$  and  $\varphi_{0b} - \frac{\pi}{2}$ , respectively.

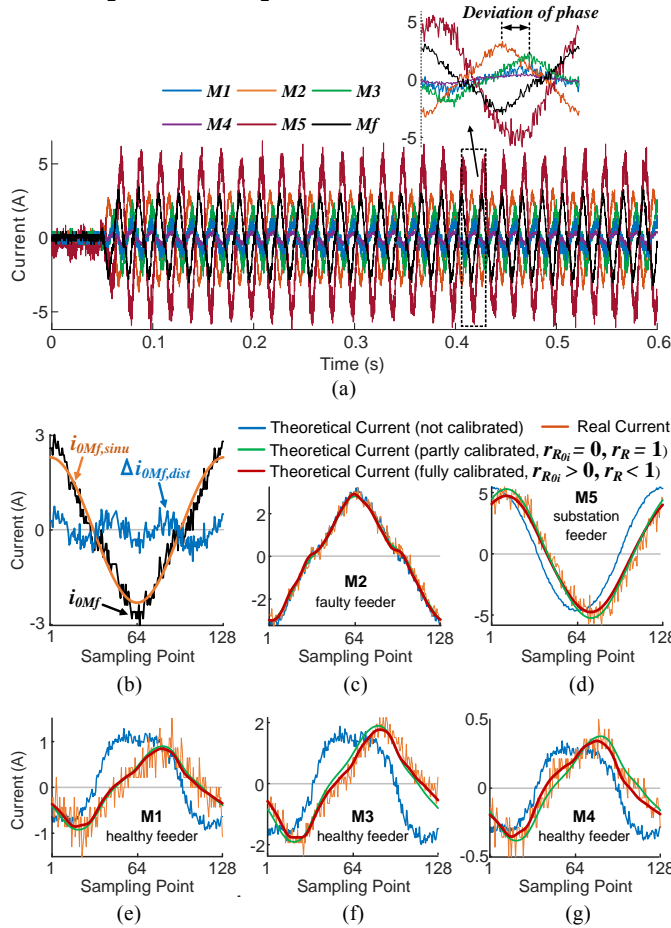


Fig.8 Comparison between real ZSCs (the HIF grounded to wet asphalt at RGN network) and the theoretical ZSCs without/calibration.

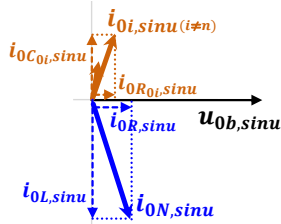


Fig.9 Phasor diagram of zero-sequence signals considering damping ratio.

Step 3: Calculate the peak amplitudes of  $i_{0i,sinu} (i \neq n)$  and  $i_{0N,sinu}$  by FFT. Then, with all phases are known, the peak amplitudes of  $i_{0C_{oi},sinu}$ ,  $i_{0R_{oi},sinu}$ ,  $i_{0L,sinu}$ , and  $i_{0R,sinu}$  can be calculated as  $A_{MC_{oi}}$ ,  $A_{MR_{oi}}$ ,  $A_{ML}$ , and  $A_{MR}$ , respectively.

Step 4: With the peak amplitudes in Step 3, calculate  $v$  and  $d$  according to (14) and (25), as well as  $r_{R_{oi}}$ ,  $r_R$  and  $c_i$ . Finally, the theoretical ZSCs at different feeders are calculated by (28)~(30) and presented in Fig.8 (c)~(g). Only the harmonics below the 11<sup>th</sup> order ( $k \leq 11$ ) are considered.

In Fig.8 (c)~(g), green curves are the ZSCs only considering the resistive component of Petersen coil ( $r_{R_{oi}}=0, r_R=1$ ), whereas the red curves also consider the line-to-ground resistances ( $r_{R_{oi}}>0, r_R<1$ ). Compared to the waveforms without calibration, the calibrated curves show much more satisfying fitting results. Besides, the accuracy can be further improved

after considering the line-to-ground resistance.

## V. APPLICATION IN FEEDER IDENTIFICATION

Based on the above analyses, there may have two ways for feeder identification: phase relationship and distortion shape.

Many algorithms detect HIFs based on the 3<sup>rd</sup> harmonic component as it is the dominant cause of current nonlinearity. For example, a traditional HIFAS system built up by Nordon Technologies [3] and T. Cui's work [7] both believe that the phase difference between the fundamental current and the 3<sup>rd</sup> harmonic current (denoted as  $\Delta\varphi_{I1-I3}$ ) is around  $180^\circ$  (e.g.,  $180^\circ \pm 40^\circ$ ) at the fault area. This well-known fault information reveals an original nonlinearity feature of HIF, inspiring many further algorithms based on distortions and time-frequency distributions. These approaches are effective to identify the feeder of HIF when the damping ratio is small, like Fig.6.

However, with the theories introduced in this paper, we can make a confident judgment that the above algorithms cannot work under many fault conditions, for the following two factors:

*Factor 1*): the diversity of distortions introduced in Section II, especially the phenomenon of 'distortion offset', could make the above methods invalid. For example,  $\Delta\varphi_{I1-I3}$  is about  $267.8^\circ$  and  $255.6^\circ$  for the HIFs in Fig.4 (f) and (g), respectively.

*Factor 2*), the existence of the damping ratio make it unreliable to distinguish between the faulty feeder and healthy feeders only by  $\Delta\varphi_{I1-I3}$ . Denote the  $\Delta\varphi_{I1-I3}$  at the healthy feeder  $i$  as  $\Delta\varphi_{0i,I1-I3}$ , and at the fault point as  $\Delta\varphi_{0f,I1-I3}$ . To simplify analyses, line-to-ground resistances are neglected ( $r_{R_{oi}}=0$ ). Then, according to (29),  $\Delta\varphi_{0i,I1-I3}$  is expressed as:

$$\begin{aligned} \Delta\varphi_{0i,I1-I3} &= 3\theta_{sinu} - \theta_{dist}^{(H,3)} + \Delta\varphi_{0f,I1-I3} \\ &= 3 \left[ 180^\circ + \arctan\left(\frac{d}{v}\right) \right] - \arctan\left(\frac{3d}{8+v}\right) + \Delta\varphi_{0f,I1-I3} \end{aligned} \quad (31)$$

When considering the *Factor 1*), we can set  $\Delta\varphi_{0f,I1-I3} \in [180^\circ - 40^\circ, 267.8^\circ + 40^\circ]$ . In (31), it can be calculated that  $3 \left[ 180^\circ + \arctan\left(\frac{d}{v}\right) \right] - \arctan\left(\frac{3d}{8+v}\right) \in [-100^\circ, 180^\circ]$ , when  $v \in [-0.1, 0)$  and  $d \in [0, 0.5]$ . Then,  $\Delta\varphi_{0i,I1-I3}$  should be in the range of  $[40^\circ, 487.8^\circ)$ , which means it could be any angle and even equal to that of the faulty feeder. In conclusion, just  $\Delta\varphi_{I1-I3}$  cannot guarantee the reliability of feeder identification. Improvements are needed.

When utilizing the phase relationship, the 3<sup>rd</sup> harmonic is still the most encouraged, as other harmonics are much smaller and will bring more errors. Based on the theories in this paper, the faulty feeder can be identified as follows:

For a feeder  $n$  and another feeder  $i$  ( $i \neq n$ ), make a judgment that whether the requirement in (32) is satisfied. If it is satisfied for all feeders, the feeder  $n$  will be regarded as the faulty feeder.

$$Indicator = |\Delta\varphi_{0n,U1-I3} - \Delta\varphi_{0i,U1-I3} - 180^\circ| \leq Thr \quad (32)$$

where,  $\Delta\varphi_{0X,U1-I3}$  is the phase difference between the fundamental ZSV and the 3rd harmonic ZSC at feeder  $X$  ( $X=i, n$ ). Specifically,  $\Delta\varphi_{0X,U1-I3} = 3\Delta\varphi_{0X,U1-I1} + \Delta\varphi_{0X,I1-I3}$ , where  $\Delta\varphi_{0X,U1-I1}$  represents the phase difference between the fundamental ZSC and ZSV. Then, (32) can be expressed as:

$$Indicator = \left| \theta_{0n,dist}^{(H,3)} - \theta_{0i,dist}^{(H,3)} - 180^\circ \right| \leq Thr \quad (33)$$

where,  $\theta_{0n,dist}^{(H,3)}$  and  $\theta_{0i,dist}^{(H,3)}$  are the  $\theta_{dist}^{(H,3)}$  in (28) and (29).

To better understand the performance of the proposed indicator, we extend the ranges of  $\nu$  and  $d$  as  $\nu \in [-0.4, 0]$  and  $d \in [0, 1]$ , curves of the indicator are shown in Fig.10, where  $Thr=40^\circ$ . On the one hand, the indicator is not affected by the aforementioned *Factor 1*). On the other hand, when  $c_n$  is smaller than 0.4, the proposed ‘indicator’ is effective for all the  $\nu$  and  $d$ .

As the increase of  $c_n$ , the effective area will be narrowed. However,  $c_n \geq 0.6$  is not a common condition, which means the length of faulty feeder is larger than the total lengths of the other feeders. Even so, the problem can still be figured out by deploying more devices at the long feeder and dividing it into several areas. Then, the area where fault happens can be regarded as the faulty feeder, and other areas can be regarded as healthy feeders. Deducing and conclusions are still valid.

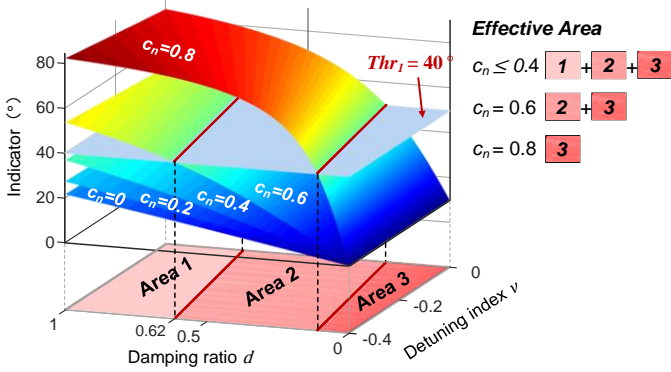


Fig.10 Effective area of the proposed ‘indicator’.

Fig.11 presents the effective area of the widely used approach that we have mentioned above. For the faulty feeder, the threshold of (31) is set as  $|\Delta\varphi_{0n,I1-I3} - \Delta\varphi_{0f,I1-I3}| \leq 40^\circ$ . For healthy feeders, they should not be wrongly identified as the faulty feeder, so that:  $|\Delta\varphi_{0i,I1-I3} (i \neq n) - \Delta\varphi_{0f,I1-I3} - 180^\circ| > 40^\circ$ . The arrows in Fig.11 represents the directions that the criteria are satisfied. Comparing Fig.10 with Fig.11, the proposed indicator present conspicuous improvements.

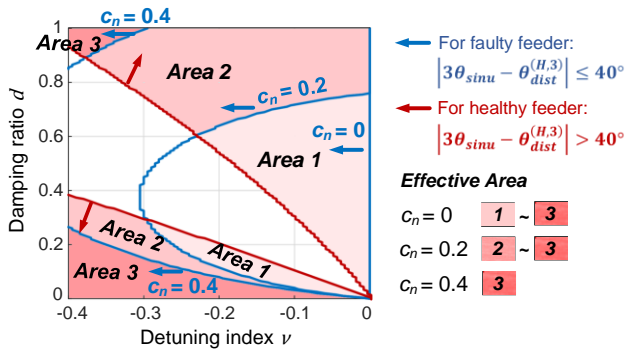


Fig.11 The effective area of a widely used traditional approach. *Factor 1*) is not considered and  $\Delta\varphi_{0f,I1-I3}$  is simplified as a constant  $180^\circ$ .

Another category of algorithms that is prospectively effective for feeder identification is based on the distortion shape [12],[20]. Compared to phase-based approaches, the distortion-based approaches perform better in anti-noise ability and

reducing the effects of measuring errors. Due to the page limitation, detailed introductions of how to improve this category of approaches cannot be presented. In brief, the improvements can also be inspired by (32), as the 3<sup>rd</sup> harmonic is the dominant cause of distortion.

## VI. CONCLUSION

This paper provides a theoretical basis to reveal the essential features of HIFs at different feeders, and help find out the most suitable fault information for feeder identification.

1) Based on the energy balance theory, the diversity of non-linear distortion is explained and confirmed by real HIFs;

2) Characteristics of distortions and phase relationships are theoretically deduced. Both the effects of detuning index and damping ratio at practical networks are considered. Conclusions are all verified by real HIF. The theories in this paper help understand the relationship between different ZSC components, catch the essential differences between feeders, and provide solid guidance to more reliable approaches;

3) A specific phase relationship based on the fundamental ZSV and the 3<sup>rd</sup> harmonic ZSC is suggested as the fault information and formed as a universally reliable indicator. The phase-based indicator can also be used to inspire other categories of algorithms.

## REFERENCE

- [1] A. Ghaderi, et al, "High-Impedance Fault Detection in the Distribution network Using the Time-Frequency-Based Algorithm," *IEEE Trans. Power Del.*, vol. 30, no. 3, pp. 1260-1268, Jun. 2015.
- [2] M. Mishra, and R. R. Panigrahi, "Taxonomy of high impedance fault detection algorithm," *Measurement*, vol. 148, 106955, 2019.
- [3] Power System Relaying Committee, Working Group D15 of the IEEE Power Eng. Soc., "High impedance fault detection technology," Mar. 1996.
- [4] CIGRE Study Committee B5, Report of Working Group 94, "High impedance faults," Jul. 2009.
- [5] D. P. S. Gomes, et al. "The effectiveness of different sampling rates in vegetation high-impedance fault classification," *Electr. Power Syst. Res.*, vol. 174, 2019.
- [6] A. Ghaderi, H.L. Ginn III and H. A. Mohammadpour. "High impedance fault detection: A review." *Elec. Power Syst. Res.*, 143: pp: 376-388, 2017.
- [7] T. Cui, X. Dong, Z. Bo and S. Richards, "Integrated scheme for high impedance fault detection in MV distribution system," *2008 IEEE/PES Transmission and Distribution Conference and Exposition: Latin America, Bogota, 2008*, pp. 1-6.
- [8] D. P. S. Gomes, C. Ozansoy and A. Ulhaq, "High-Sensitivity Vegetation High-Impedance Fault Detection Based on Signal's High-Frequency Contents," *IEEE Trans. Power Del.*, vol. 33, no. 3, pp. 1398-1407, Jun. 2018.
- [9] Y. Xue, et al., "Resonance Analysis and Faulty Feeder Identification of High-Impedance Faults in a Resonant Grounding System," *IEEE Trans. Power Del.*, vol. 32, no. 3, pp. 1545-1555, June 2017.
- [10] A. Nikander, and P. Jarventausta, "Identification of High-Impedance Earth Faults in Neutral Isolated or Compensated MV Networks," *IEEE Trans. Power Del.*, vol. 32, no. 3, pp. 1187-1195, Jun. 2017.
- [11] M. Wei, et al., "High Impedance Arc Fault Detection Based on the Harmonic Randomness and Waveform Distortion in the Distribution System," *IEEE Trans. Power Del.*, vol. 35, no. 2, pp. 837-850, April 2020.
- [12] M. Michalik, et al., "High-impedance fault detection in distribution networks with use of wavelet-based algorithm," *IEEE Trans. Power Del.*, vol. 21, no. 4, Oct. 2006.
- [13] X. Wang et al., "High Impedance Fault Detection Method Based on Variational Mode Decomposition and Teager-Kaiser Energy Operators for Distribution Network," *IEEE Trans. Smart Grid*, vol. 10, no. 6, pp. 6041-6054, Nov. 2019.
- [14] C. Gonzalez, et al. "Directional, High-Impedance Fault Detection in Isolated Neutral Distribution Grids." *IEEE Trans. Power Del.*, vol. 33, no. 5, Oct. 2018.
- [15] T. Tang, et al. "Single-phase high-impedance fault protection for low-resistance grounded distribution network," *IET Gener. Transm. Distrib.*, vol. 12, no. 10, pp. 2462-2470, 2018.
- [16] K. Pandakov, H. K. Hoidalén, and S. Traetteberg, "An Additional Criterion for Faulty Feeder Selection During Ground Faults in Compensated Distribution Networks," *IEEE Trans. Power Del.*, vol. 33, no. 6, pp. 2930-2937, 2018.
- [17] T. Y. Li, Y. D. Xue and B. Y. Xu, "High-impedance fault detection technology based on transient information in a resonant grounding system," *CIGRE - Open*

*Access Proceedings Journal*, vol. 2017, no. 1, pp. 1176-1179, 10 2017.

- [18] Y. Xue, et al., "Practical Experiences with Faulty Feeder Identification Using Transient Signals," IET 9th International Conference on Developments in Power System Protection, Glasgow, 2008, pp. 720-723.
- [19] M. Wei, et al., "Distortion-Controllable Arc Modelling for High Impedance Arc Fault at the Distribution Network," *IEEE Trans. Power Del.*, 2020.
- [20] M. Wei, et.al., "Distortion-Based Detection of High Impedance Fault in Distribution Systems," *IEEE Trans. Power Del.*, 2020.